

# A Lithium–Sulfur Battery using a 2D Current Collector Architecture with a Large-Sized Sulfur Host Operated under High Areal Loading and Low E/S Ratio

Matthew Li, Yining Zhang, Zhengyu Bai,\* Wen Wen Liu, Tongchao Liu, Jihyeon Gim, Gaopeng Jiang, Yifei Yuan, Dan Luo, Kun Feng, Reza S. Yassar, Xiaolei Wang, Zhongwei Chen,\* and Jun Lu\*

While backless freestanding 3D electrode architectures for batteries with high loading sulfur have flourished in the recent years, the more traditional and industrially turnkey 2D architecture has not received the same amount of attention. This work reports a spray-dried sulfur composite with large intrinsic internal pores, ensuring adequate local electrolyte availability. This material offers good performance with a electrolyte content of  $7 \mu\text{L mg}^{-1}$  at high areal loadings ( $5\text{--}8 \text{ mg cm}^{-2}$ ), while also offering the first reported  $2.8 \mu\text{L mg}^{-1}$  ( $8 \text{ mg cm}^{-2}$ ) to enter into the second plateau of discharge and continue to operate for 20 cycles. Moreover, evidence is provided that the high-frequency semicircle (i.e., interfacial resistance) is mainly responsible for the often observed bypassing of the second plateau in lean electrolyte discharges.

Lithium–sulfur batteries (LSBs) have recently gained tremendous amount of academic and industrial interest due to its extremely high theoretical energy density ( $2500 \text{ Wh kg}^{-1}$ )<sup>[1]</sup> and the natural abundance of sulfur. However, technical challenges such as the well-known polysulfide (PS) shuttle effect, volume expansion, and electrically insulating nature of sulfur have hinders it widespread application.<sup>[2]</sup> Much focus has been placed on the cathode material,<sup>[3]</sup> separator,<sup>[4]</sup> and electrolyte,<sup>[5]</sup> subsystems of LSB with impressive levels of success at both low ( $<2 \text{ mg cm}^{-2}$ ) and high ( $>4 \text{ mg cm}^{-2}$ ) sulfur areal loadings. Recent trends in the literature reveal a large emphasis on the electrolyte to sulfur ratio (E/S) due to its large impact

on the overall energy density of the LSB cell.<sup>[6,7]</sup> As a benchmark, Hagen et al.<sup>[8]</sup> among others<sup>[9]</sup> have noted that even with an extremely low  $E/S = 3$  the projected energy density would just match that of the current lithium-ion battery (LIB) technologies. As the performance of LSB drastically decreases with decreasing electrolyte volumes, there are almost no published reports reaching  $E/S$  levels below 3. One of the key challenges in achieving low  $E/S$  ratio lies in enhancing the electrode's ability to access the electrolyte. This is a major factor influencing the observed excellent performance of the many backless freestanding electrodes (BFE).<sup>[10,11]</sup> BFE electrodes have at least double the pore openings (front and back) to access the electrolyte residing in the various free space of the coin cell while traditional 2D blade-cast electrode only have one opening. In addition to scalability issues such as electrode manufacturing, in-plane electron transfer, and electrodes to tab welding procedure,<sup>[12]</sup> the advantages of the BFE designs over the 2D electrode might not carry over to the other battery cell configurations (pouch cell, cylindrical) where void spaces are mostly eliminated for compactness.

While the 2D electrode configuration is likely commercially imperative, their single sided, purely microporous/mesoporous

M. Li, T. Liu, Dr. J. Gim, Dr. Y. Yuan, Dr. J. Lu  
Chemical Sciences and Engineering Division  
Argonne National Laboratory  
9700 Cass Ave, Lemont, IL 60439, USA  
E-mail: junlu@anl.gov

M. Li, Dr. Y. Zhang, Dr. W. W. Liu, Dr. G. Jiang, D. Luo, Dr. K. Feng,  
Prof. Z. Chen  
Department of Chemical Engineering & Waterloo Institute of  
Nanotechnology  
University of Waterloo  
200 University Ave West, Waterloo, ON N2L 3G1, Canada  
E-mail: zhwenchen@uwaterloo.ca

 The ORCID identification number(s) for the author(s) of this article can be found under <https://doi.org/10.1002/adma.201804271>.

DOI: 10.1002/adma.201804271

Prof. Z. Bai  
School of Chemistry and Chemical Engineering  
Key Laboratory of Green Chemical Media and Reactions  
Ministry of Education  
Henan Normal University  
Xinxiang 453007, China  
E-mail: baizhengyu@htu.edu.cn

Dr. Y. Yuan, Prof. R. S. Yassar  
Department of Mechanical and Industrial Engineering & Department of  
Civil and Materials Engineering  
University of Illinois at Chicago  
842 W. Taylor Street, Chicago, IL 60607-7022, USA

Prof. X. Wang  
Department of Chemical and Materials Engineering  
Concordia University  
1455 Boulevard de Maisonneuve O, Montréal, QC H3G 1M8, Canada

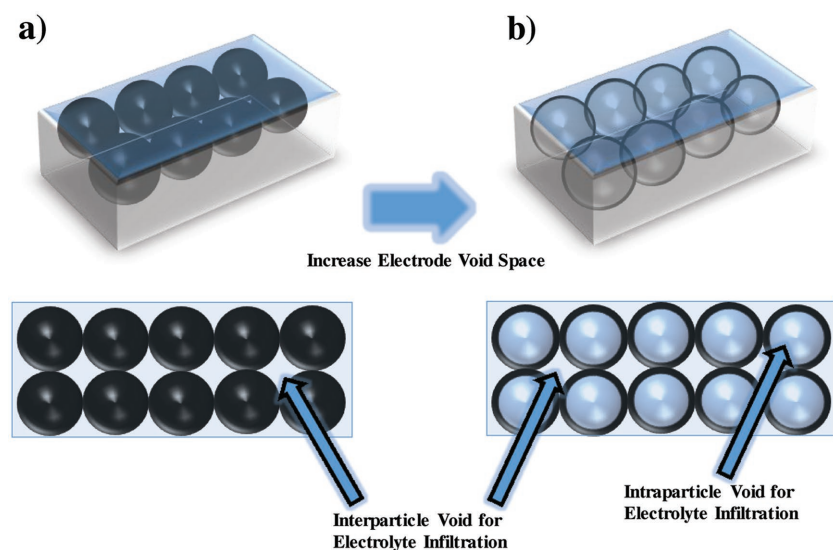


**Figure 1.** a,b) Schematics of a low-porosity electrode with nonhollow material (a) and a high-porosity electrode with micrometer-sized hollow material (b).

sulfur hosts will form an overall porous structure with low void space for electrolyte, as illustrated in **Figure 1a**. As a result, 2D current collectors have a much smaller presence in the overall field of high loading sulfur electrodes. However, if the microporous/mesoporous sulfur hosts were made with large intrinsic voids, as envisioned in **Figure 1b**, the intrinsic macroporous void space can act as an extra electrolyte reservoir for enhancing electrolyte accessibility. In this way, some of the main benefits of BFEs can be transferred to the 2D electrode configuration. Unfortunately, because the term macroporosity is commonly associated with bulkiness, fluffiness, and ultimately impracticality, this might be preemptively dismissed as an invalid strategy toward lean E/S, as the large void spaces will be expected to demand a high E/S. Upon closer inspection, often reported electrolyte ratios of  $>10$  E/S are theoretically impossible to reside inside of the cathode and separator (the only porous non-casing components of the cell). Listed in **Table S1** (Supporting Information) are the calculated theoretical upper limit for E/S ratios of a few publications with reported electrode thickness. This simple analysis indicates that the performance enhancements observed by many works where E/S is increased are only physically achievable due to the extra void space in the coin cell, which are not available in the pouch/cylindrical cell configurations.

To this end, we look to increase the porosity of the electrode with large sized hollow material of macrosized diameters (i.e., intrinsic macropores), replicating the main beneficial features of 3D current collector designs. This type of material poses as a particularly attractive sulfur host material for the 2D electrode configuration under lean E/S. The large intrinsic internal voids should be excellent for providing local electrolyte reservoirs that can serve to lower the electrolyte viscosity, which would be ideal for low-electrolyte-high-loading sulfur electrodes. However, most particle sizes ( $<1 \mu\text{m}$ ) are relatively small, which would create small interparticle pores (poor “bulk” electrolyte Li-ion transfer), voiding any advantages gained from its hollow nature

at higher areal sulfur loadings. Furthermore, it is well known that it is difficult to achieve robust high loading electrode when using a cathode active composite that has high surface area.<sup>[13]</sup> To solve these problems there are numerous work in the LIB and LSB fields investigating techniques to produce secondary particles with the same advantages of nanosized morphologies while mitigating the disadvantages (reduced exposed surface area). These techniques can be considered quite mature in the field of 2D-electrode-based high-areal-sulfur-loading LSBs.<sup>[13–16]</sup>

Our chosen agglomeration technique, spray drying,<sup>[17]</sup> (shown in **Figure 2a**) is widely used in many different industries due to its high throughput production capabilities. Specifically in this work, we first synthesized hollow porous carbons (HPC) with a large core,<sup>[18]</sup> loaded sulfur via the melt diffusion method and spray dried with graphene oxide at  $200 \text{ }^\circ\text{C}$  (nozzle temperature) forming what we define as spray dried hollow porous

carbon (SDHPC). The large droplet size of the atomized feed solution ensures the formation of secondary particles while the graphene oxide acts as structural support. After heat treatment in an Ar filled autoclave at  $230 \text{ }^\circ\text{C}$  for 12 h (GO reduction), the final SDHPC electrode material is obtained. To estimate the sulfur content in SDHPC, the mass change in GO must be first accounted for. Thermal gravimetric analysis (TGA) of GO in  $\text{N}_2$  reveals that the stabilized mass percent did not vary appreciably between  $200$  and  $250 \text{ }^\circ\text{C}$  (**Figure 2b**) indicating that the mass of SDHPC should have stabilized during the 12 h  $230 \text{ }^\circ\text{C}$  heat treatment in alignment with the literature.<sup>[19]</sup> Accordingly, TGA of SDHPC after heat treatment only shows a single inflection (single peak in the rate of wt% change, **Figure 2c**) with a plateau starting at  $\approx 30$  wt% at around  $250 \text{ }^\circ\text{C}$  suggesting a sulfur loading of  $\approx 70\%$ . This is in good alignment with the theoretical  $68\%$  calculated based on a HPC75S to GO mass ratio of 5:1 (spray-dryer feed) with a  $50\%$  mass retention of GO after the  $230 \text{ }^\circ\text{C}$  heat treatment. The morphology of SDHPC is shown under scanning electron microscopy (SEM) in **Figure 2d,e**, respectively, indicating the successful wrapping of graphene and the agglomeration of HPC into larger particles (SDHPC). The broad particle size distribution is due to the centrifugal based collection mechanism of the spray dryer’s cyclone<sup>[20]</sup> and could aid in the performance of the cell as shown in previous work.<sup>[14,21]</sup> Moreover, transmission electron microscopy (TEM, **Figure 2f**) indicates that the graphene is wrapped throughout the structure of the secondary particle, providing an electron-conducting pathway. At higher magnifications (**Figure 2g**), the graphene is shown encapsulating the HPC primary particles. More importantly, the large intrinsic  $\approx 500 \text{ nm}$  voids of the hollow structures can be clearly found intact throughout the large secondary particle. Energy-dispersive X-ray spectroscopy mapping of C, N, O, and S (**Figure S1a,b**, Supporting Information) further indicates that there are indeed large internal void throughout SDHPC and sulfur mostly resides in the wall of these voids. The existence of these internal voids is the most

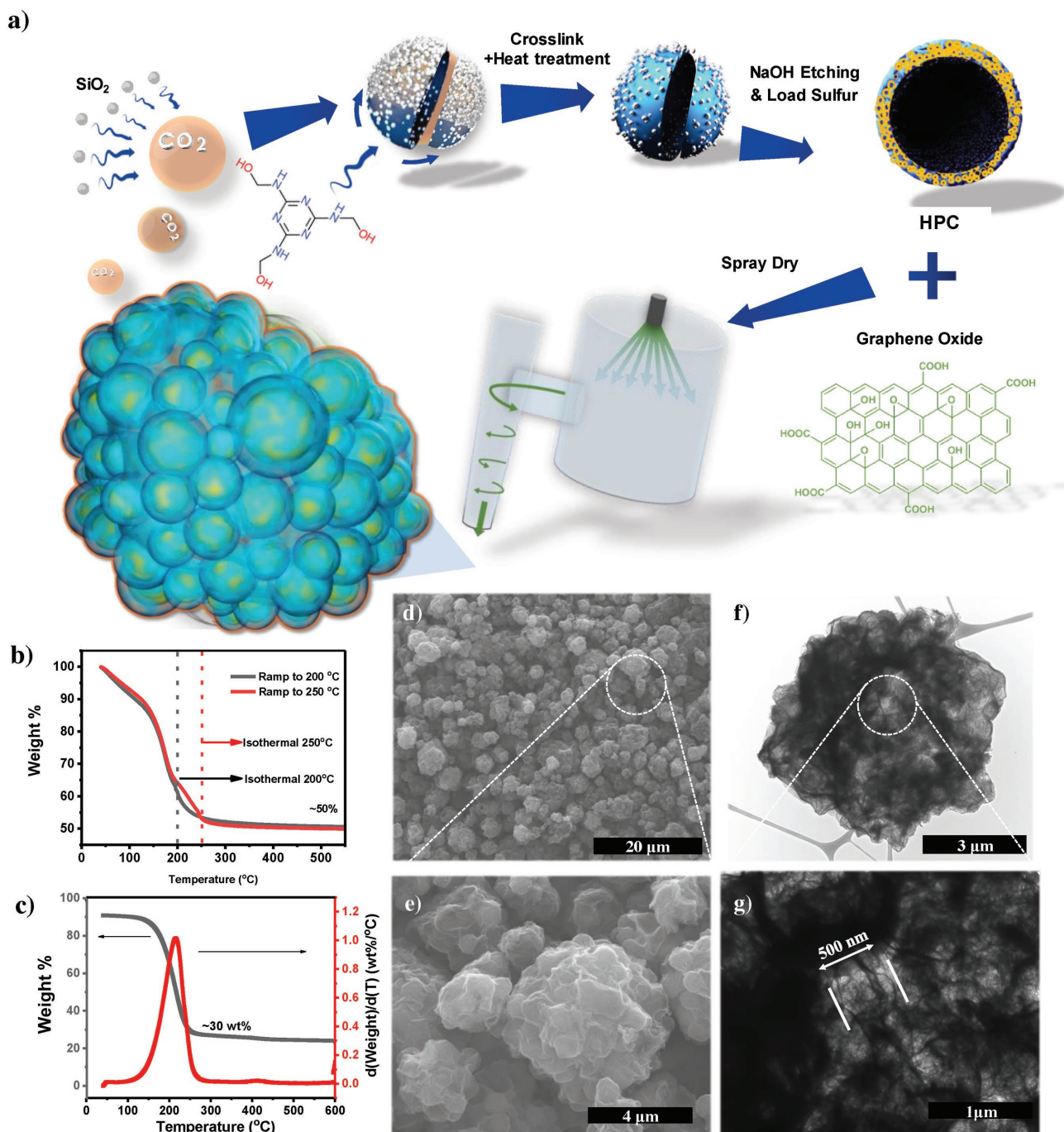


**Figure 2.** a) Schematic of the synthesis process of SDHPC, b) TGA curves of graphene oxide ramping to 200 and 250  $^{\circ}\text{C}$  followed by holding isothermal for 2 h, c) TGA curves of SDHPC after heat treatment, d) low- and e) high-magnification SEM images and f) low- and g) high-magnification TEM image of SDHPC after spray drying and 230  $^{\circ}\text{C}$  heat treatment.

beneficial difference between SDHPC and other reported spray dried sulfur composites. These voids will serve as guaranteed intrinsic void spaces (shown in Figure 1b) throughout the electrode to provide electrolyte accessibility to sulfur even at low electrolyte ratios.

To confirm the infiltration of electrolyte into the voids, an electrolyte absorption test is performed. The test entailed the micropipetting of precisely 4  $\mu\text{L}$  of electrolyte (0.2 M  $\text{LiNO}_3$

and 1 M  $\text{LiTFSI}$  in 1,3 dioxolane and dimethoxyethane at 1:1 v/v) onto a circular 15 mm diameter electrode (HPC and SDHPC, **Figure 3a**). The event was filmed and the time difference between initial contact and final absorption of the droplet is defined as the absorption time. By measuring the height of the droplet over time, a time-resolved absorption profile of the electrolyte could be observed. The larger particle size of SDHPC should create larger interparticle pores,<sup>[13–16]</sup> which

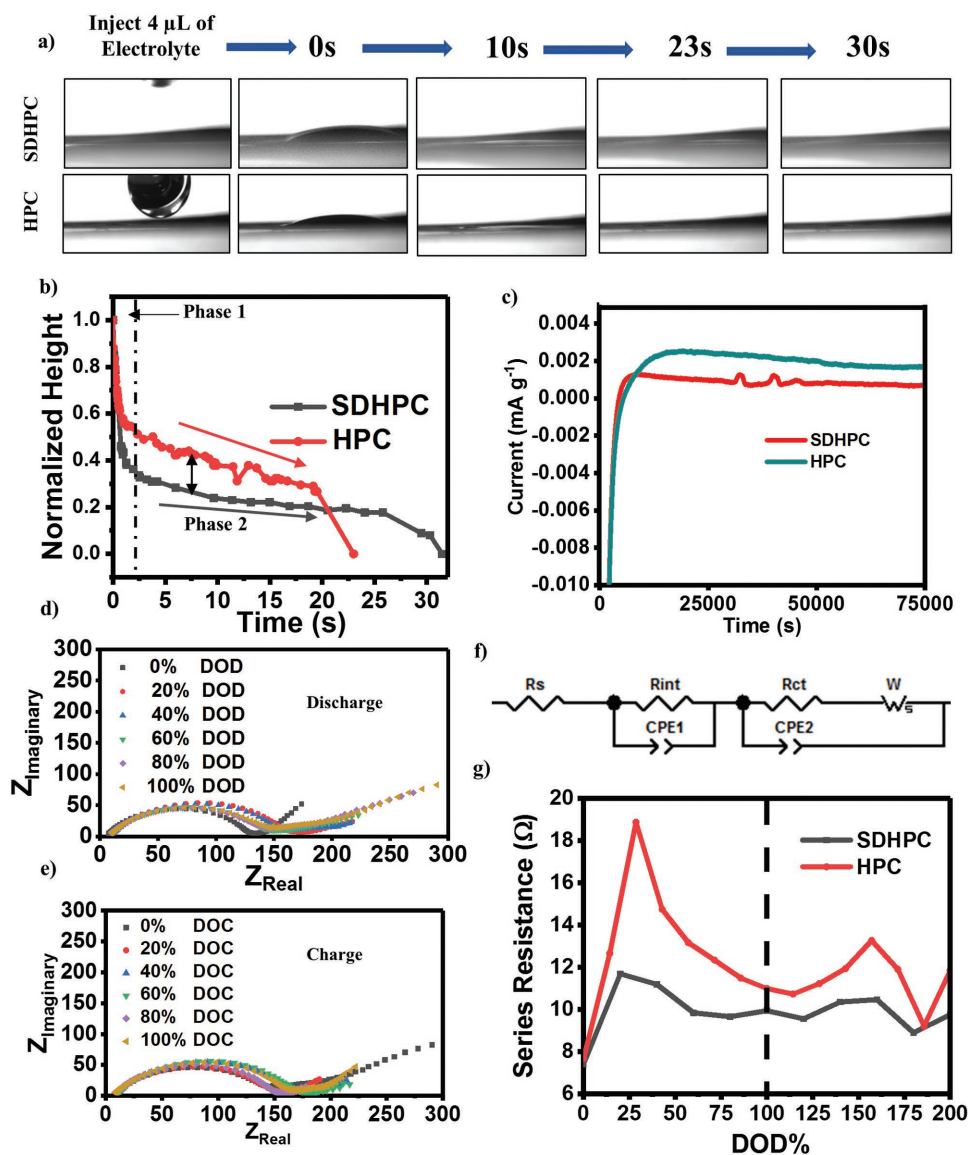


**Figure 3.** a) Image sequence of the injection and absorption of 4  $\mu\text{L}$  of electrolyte into SDHPC and HPC electrodes, b) corresponding droplet height versus time profile and c) shuttle current measurement of both SDHPC and HPC. d) Discharge and e) charge EIS spectrums of SDHPC electrode at different DOD, f) equivalent circuit model used for fitting impedance data. g) Fitted values of series resistance plotted versus DOD. Note that 0–100% DOD represents discharge while 100–200% DOD represent charge.

is expected to decrease electrolyte wetting time.<sup>[22]</sup> Interestingly, it was found that the total wetting time of SDHPC (larger interparticle pores) was  $\approx 31$  s whereas HPC (smaller interparticle pores) only took  $\approx 23$  s, indicating that HPC absorbed the electrolyte slightly quicker. This result offers us with valuable insight into the pore structure of the SDHPC electrode. Both absorption processes appear to proceed in a two-step manner (Figure 3b). It is well known that liquid (electrolyte) infiltration into a porous media (electrode) of the electrode depends on the apparent contact angle between the electrolyte and the particles, characteristic of electrode pore network and the pressure differential.<sup>[22]</sup> The initial rapid drop (labeled Phase 1) is followed by a slower plateaued infiltration region (label Phase 2) for both samples. The initial quick absorption profile is due to the pressure head produced by the height of the droplet. As the droplet

is absorbed, the pressure head (a component of the driving force responsible for infiltration) will decrease to the point where it is slowed by the smaller pores in the electrode. During this slowing process, the height of the droplet will possess a more plateaued time profile. There are two distinct differences between SDHPC and HPC. First, the initial decrease in height for SDHPC was much more than HPC, this is most likely due to the larger interparticle pores of the electrode.<sup>[13,14]</sup> Second, the slope of the plateau for SDHPC is noticeably lower than that of HPC. We believe the smaller slope of SDHPC might suggest that the rGO hindered the infiltration of electrolyte into agglomerated hollow structures of SDHPC. With an increased sulfur loading, the PS retention capability of the host must be enhanced compared to the lower loadings. From the delayed infiltration of electrolyte into SDHPC, we note that it could

imply a tortuous liquid pathway into SDHPC. As such, this could be beneficial in limiting the outwards diffusion of PS. Indeed, from our shuttle current measurements (Figure 3c), SDHPC possessed a significantly lower steady state current signal ( $0.747 \mu\text{A g}^{-1}$ ) compared to HPC ( $1.68 \mu\text{A g}^{-1}$ ) at the same areal loading ( $2.5 \text{ mg cm}^{-2}$ ). To further demonstrate the ability of SDHPC to limit PS outwards diffusion, we performed in situ electrochemical impedance spectroscopy (EIS) experiments on both HPC and SDHPC ( $2.5 \text{ mg cm}^{-2}$ ) as a function of state of charge/discharge (DOD, 0–100% represents discharge while 100–200% represents charge). According to the Nyquist plot for both discharge and charge of SDHPC shown in Figure 3d,e, respectively, there appears to be a drastic change in cell impedance throughout discharge and charge. After fitting to a circuit model (Figure 3f),<sup>[18,23,24]</sup> the series resistance versus DOD is shown in Figure 3g. The series resistance is found to increase until 25–30% DOD followed by a steady decrease into the end of discharge. During charge, the series resistance steadily increases again, peaking at  $\approx 160$  DOD followed by a decrease until the end of charge, which is corroborated by the literature.<sup>[18,24,25]</sup> Interestingly, throughout discharge and charge the series resistance of HPC was higher than SDHPC. For LSB, changes in the series resistance are usually attributed to the resistance of the electrolyte, and increases with increasing polysulfide concentration.<sup>[26]</sup> Therefore, our results suggest that SDHPC is able to limit the polysulfide concentration in the bulk electrolyte more effectively than HPC, which corroborates well with the electrolyte absorption and shuttle current measurements.

The combined benefits of the macroporous internal electrode structure in addition to the high PS limiting capabilities of SDHPC is reflected in its electrochemical performances. Figure 4a shows the rate performance of this SDHPC from 0.1 to 5 C, demonstrating exceptional electrochemical activity with a discharge capacity of  $\approx 500 \text{ mAh g}^{-1}$  at 5 C even at an appreciable sulfur loading ( $2.5 \text{ mg cm}^{-2}$ ). SDHPC is found to be able to recover the majority of its original 0.1 C capacity in addition stable cycling until the 100th cycles at 1 C. Figure 4b,c displays the cycle stability of electrodes at 5 and 6  $\text{mg cm}^{-2}$  with  $7 \mu\text{L mg}^{-1}$  of electrolyte at 0.05 C for the first five cycles followed by 0.1 C. Figure 4d presents the cycle stability of 8  $\text{mg cm}^{-2}$  electrodes also with  $7 \mu\text{L mg}^{-1}$  of electrolyte but cycled at 0.05 C. The corresponding voltage profiles for the 5, 6, and 8  $\text{mg cm}^{-2}$  cells are shown in Figure 4e,g, respectively. Both cells achieved a first cycle discharge of about  $\approx 1200 \text{ mAh g}^{-1}$ . While the 5  $\text{mg cm}^{-2}$  cells were able to maintain relatively stable cycling upward of 280 cycles, the 6  $\text{mg cm}^{-2}$  experienced a significant decrease in capacity at about the 105th cycle but remained stable afterward upward of 200 cycles. We believe that the sudden drop in capacity is related to the serious corrosion of the Li anode (post cycling SEM shown in Figure S1, Supporting Information). It should be noted that no sudden drop in capacity is observed for the 8  $\text{mg cm}^{-2}$  cell, which is most likely due to the lower current density.<sup>[27]</sup> In terms of 2D blade-cast electrode, at this areal loading and lean electrolyte conditions, this performance is quite exceptional compared to recent works.<sup>[7,14,16,28]</sup> When the E/S ratio is further lowered to  $2.8 \mu\text{L mg}^{-1}$ , it is found that the cell was able to cycle at a C-rate of 0.025. The voltage profile (Figure 5a) reveals a very high

discharge overpotential, dropping to nearly  $\approx 1.4 \text{ V}$  on the first cycle and  $\approx 1.75 \text{ V}$  on the second discharge process. However, if the C-rate is increased to 0.05 C the cell cannot discharge (voltage profile shown in Figure S2, Supporting Information). This is often attributed to the enormous increase in overpotential from either electrolyte viscosity (highly concentration polysulfide solution) or deposition kinetics. Work presented by Fan et al. have also reported similar results at lean electrolyte conditions.<sup>[29]</sup> The cycle life decreased rapidly compared to its excess electrolyte counterpart. This has been an intriguing phenomenon throughout the literature. Although the cycle performance is only for 20 cycles (Figure 5b), we have demonstrated here a material and conceptual design that can be cycled at a commercially viable electrolyte content. When compared to other high loading works, an electrolyte content of  $2.8 \mu\text{L mg}^{-1}$  for a 8  $\text{mg cm}^{-2}$  2D blade-cast electrode has to the best of our knowledge, never been published. Furthermore, the composite content is  $>90\%$  in the slurry formulation with very low binder content (5%) and a S content of  $\approx 70\%$  in SDHPC, indicating that the total sulfur content in the electrode is well over 60%.

Unfortunately, a discharge rate of 0.025 C is hardly practical and poses a serious question as to why there is such a high overpotential. Surprisingly, there has been little work done on understanding why high loading sulfur cathode have difficulty discharging under lean electrolyte content. To understand the cause and mechanism of the observed large overpotential prior to the second plateau, we once again performed in situ EIS on a fresh 8  $\text{mg cm}^{-2}$  electrode ( $2.8 \mu\text{L mg}^{-1}$ ) discharged under two different current densities (first at 0.05 C then at 0.01 C). Specifically, the cell was first discharged at 0.05 C where the voltage quickly reaches the cut off limits (Figure 5c) with the details of the overpotential build-up recorded by EIS. After charging back to 2.8 V, the same cell was discharged at a significantly decreased current density (0.01 C), which allowed the cell to enter readily into the second plateau region without obstruction of an overpotential dip (Figure 5c). The results were fitted according to circuit diagram validated by Deng et al.<sup>[24]</sup> In general, the fitted circuit parameters (experimental spectrums can be found in Figure S3, Supporting Information) remained quite similar between the two currents during the initial stages of discharge with variation only occurring near the end of the first plateau (onset of the large overpotential). It should be expected that when increasing the current density, the PS concentration should be much higher locally (most likely completely saturated) due to the increased rate of PS generation over PS diffusion. Although our results indicate (Figure 5d) that the series resistance of 0.01 C discharge was lower than the 0.05 C, the overall difference was not large. A similar observation is found for the charge transfer resistance (mid frequency semicircle,<sup>[24]</sup> Figure 5e). Interestingly, the interfacial resistance (high-frequency semicircle, Figure 5f with Nyquist plots shown in Figure S3a,b, Supporting Information) is found to increase drastically prior to the onset of the large overpotential for the higher current discharge. This indicates that of the three circuit elements, only interfacial resistance appears to change significantly near the high overpotential region of the discharge voltage profile. Interfacial resistance is associated with the contact resistance between electron conductors within the electrode.<sup>[24,30]</sup> It is unclear whether solely  $\text{S}_8$ ,  $\text{Li}_2\text{S}$ , or even

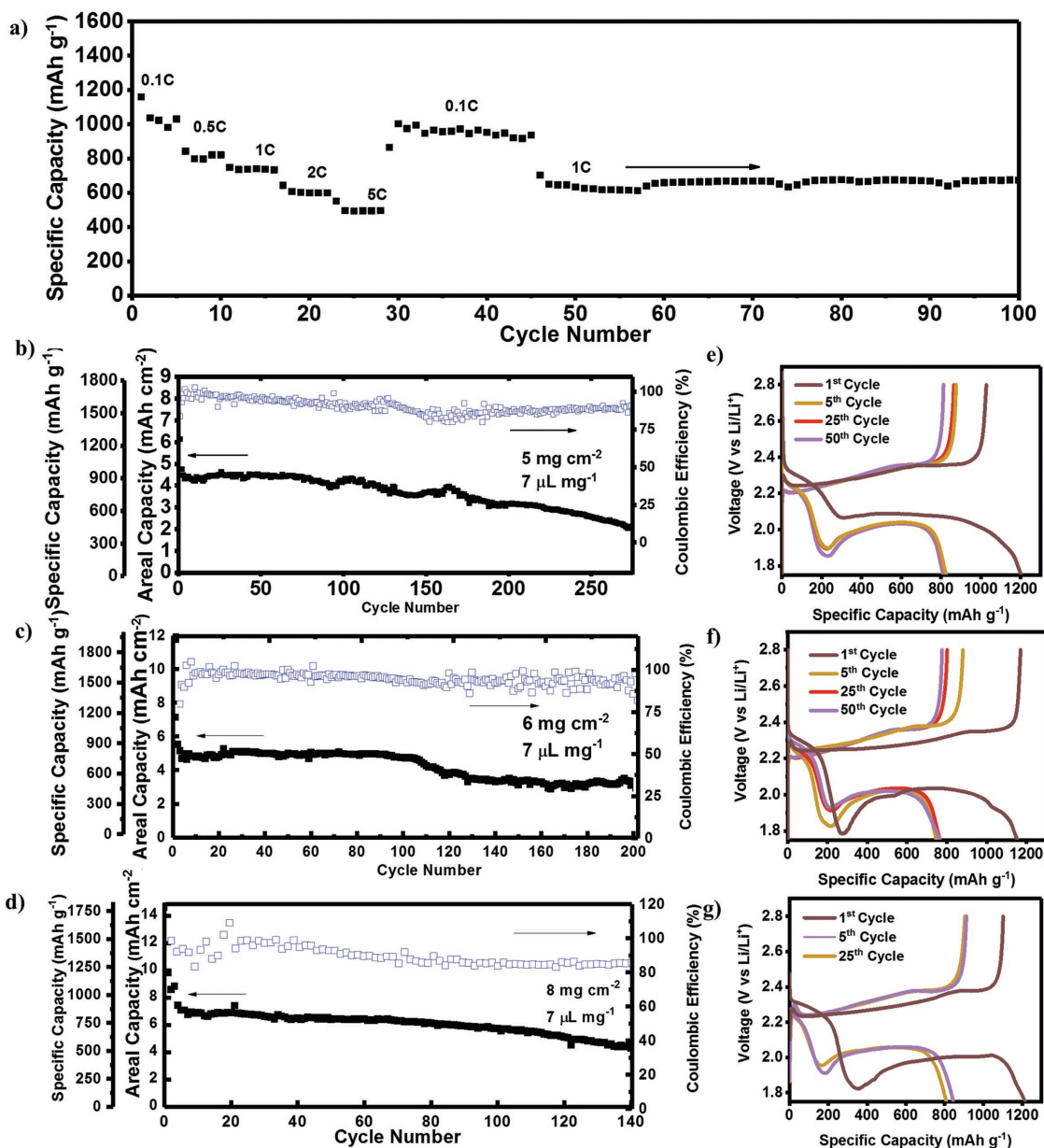


**Figure 4.** a) Rate performance of SDHPC at  $2.5 \text{ mg cm}^{-2}$  with  $7 \mu\text{L mg}^{-1}$  of electrolyte, b–d) specific capacity with Coulombic efficiency versus cycle life of SDHPC at 5, 6, and  $8 \text{ mg cm}^{-2}$  respectively and e–g) charge/discharge profiles of SDHPC at 5, 6, and  $8 \text{ mg cm}^{-2}$ , respectively. Note that 5 and  $6 \text{ mg cm}^{-2}$  cells were cycled at 0.05 C for four activation cycles before cycling at 0.1 C for the cycle life measurements while the  $8 \text{ mg cm}^{-2}$  cell was cycled at 0.05 C.

solid-state PS<sup>[31]</sup> is responsible for the large overpotential. While one might argue that the lack of capacity in the second plateau should eliminate appreciable Li<sub>2</sub>S seeding, Li<sub>2</sub>S can still form due to disproportionation reaction or direct reduction of PS onto Li (increasing interfacial resistance on Li). In an attempt to differentiate between Li<sub>2</sub>S, S and solid-state PS, we performed in situ X-ray diffraction (XRD) to monitor the crystal phase changes during the large overpotential (Figure 5g). Throughout the discharge of the first plateau and ending with a large overpotential, there are strong sulfur XRD signals with no indication of Li<sub>2</sub>S peaks. Upon closer inspection of the  $2\theta = 1.960, 2.016, 1.758,$  and  $1.670$  peak heights (Figure 5h), we concluded

that there is only a minor decrease in peak intensity with slight oscillations throughout cycling. This is in stark contrast with other reports, where a steady decrease in the sulfur diffraction pattern was observed prior to the end of the first plateau where the peaks completely disappear.<sup>[32,33]</sup> Due to the lack of any observable Li<sub>2</sub>S peaks, we suspect that the increase in interfacial resistance is not due to the deposition of Li<sub>2</sub>S. On the case of solid-state polysulfide, a recent publication has shown that the XRD pattern of polysulfides can be detected even if they were just adsorbed onto a silica surface.<sup>[33]</sup> However, no such observation was made in this work even with a nitrogen-doped polysulfide retaining carbon host,<sup>[34]</sup> which should exclude the

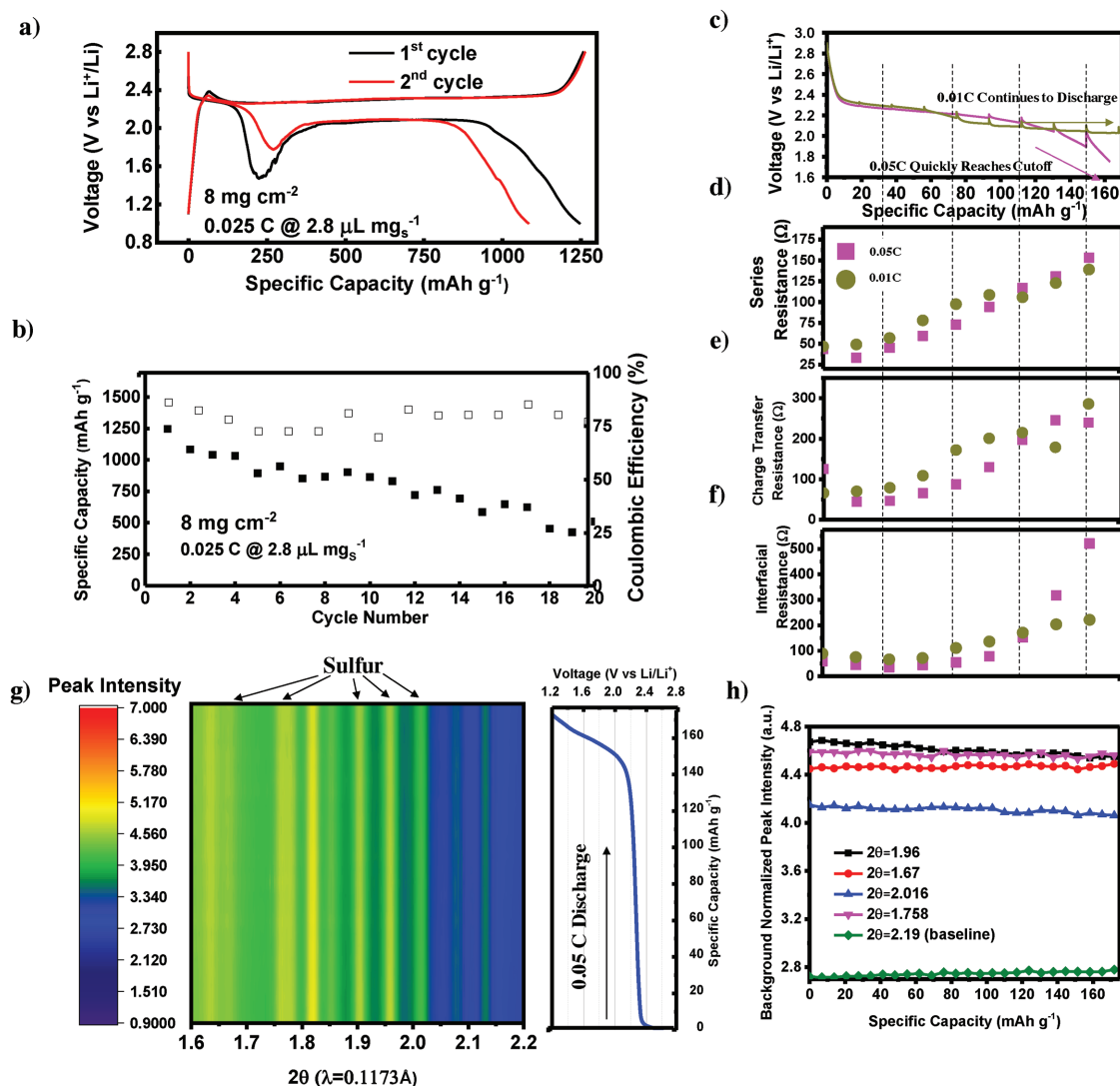


**Figure 5.** a) Charge/discharge voltage profile and b) cycling performance at 0.025 C of SDHPC. c) Voltage profile of  $8 \text{ mg cm}^{-2}$  electrode with  $2.8 \text{ } \mu\text{L mg}^{-1}$  at 0.05 and 0.01 C. Impedance data plotted as a function of specific capacity of SDHPC discharged at 0.05 and 0.01 C: d) series resistance, e) charge transfer resistance, f) interfacial resistance. g) In situ XRD contour plot of the first plateau followed by the onset of a large overpotential to 1.2 V ( $\lambda = 0.1173 \text{ \AA}$ ) and h) various peak height plotted versus discharge capacity.

possibility of solid-state polysulfide. Therefore, we believe that the high interfacial resistance is largely related to sulfur precipitation and most likely not related to solid-state polysulfide or  $\text{Li}_2\text{S}$ .

We believe that low E/S promotes solid sulfur precipitation through disproportionation reaction of concentrated high order PS. The constant regeneration of elemental sulfur deposits on already present sulfur location buffers the XRD sulfur signal, resulting in a relatively constant value. The disproportionation reaction most likely distributed sulfur locally throughout the SDHPC composite causing the observed increase in interfacial resistance. This phenomenon might be inherent to 2D current collector designs. In contrast to the BFE designs,<sup>[11]</sup> 2D current collectors are not composed of long ranged continuous conductive networks and will inevitably create multiple contact points between conductors. However, due to the need for large internal macropores, the number of these contact points

is quite low simply due to the larger particle sizes. Due to the relatively fewer contact points between the large macroporous carbons within SDHPC and between SDHPC, we believe our material and 2D current collector designs in general are more susceptible to interfacial resistance increases. Although we have shown that a macroporous 2D electrodes can achieve some cyclability at extremely low electrolyte content, its performance is still inferior to that of BFEs and therefore is not a complete solution. While this might be discouraging for 2D electrode researchers, we would like reiterate once again the enormous turnkey advantage of 2D electrodes over BFEs when time comes for prototyping.<sup>[12]</sup>

In summary, we have presented here a high-areal-loading lithium-sulfur battery (>60 wt% S in electrode) operated under lean electrolyte content (7 and  $2.8 \text{ } \mu\text{L mg}^{-1}$ ). By designing a large sized sulfur host with large intrinsic macropores encapsulated within its structure, we have enabled the stable

cycling of a blade-cast electrodes of 5, 6, and 8 mg cm<sup>-2</sup>. Even at 2.8 μL mg<sup>-1</sup>, the 8 mg cm<sup>-2</sup> electrodes demonstrated relatively stable cycling for up to 20 cycles. Furthermore, our in situ EIS and XRD analysis revealed intriguing properties pertaining to the mechanism of lean electrolyte operation and has for the first time identified that the interfacial resistance is the key impedance responsible for the electrodes to successfully entering into the second discharge plateau for high loading/lean electrolyte cells. We hope that this work will help revive and aid future work on 2D electrode-based high-energy-density lithium–sulfur batteries.

## Experimental Section

Detailed information can be found in the Experimental Section of the Supporting Information.

## Supporting Information

Supporting Information is available from the Wiley Online Library or from the author.

## Acknowledgements

M.L. and Y.Z. contributed equally to this work. J.L. gratefully acknowledges support from the Assistant Secretary for Energy Efficiency and Renewable Energy, Office of Vehicle Technologies of the U.S. Department of Energy through the Advanced Battery Materials Research (BMR) Program (Battery500 Consortium). Argonne National Laboratory is operated for DOE Office of Science by UChicago Argonne, LLC, under contract No. DE-AC02-06CH11357. The authors acknowledge financial support from the Natural Sciences and Engineering Research Council of Canada (NSERC) and the Waterloo Institute for Nanotechnology (WIN). M.L. would like to thank Andy Wan for helping in the creation of Figure 2a. Use of the Advanced Photon Source (11-ID) was supported by the US Department of Energy, Office of Basic Energy Sciences.

## Conflict of Interest

The authors declare no conflict of interest.

## Keywords

aerosols, batteries, high mass loading, low E/S ratio, sulfur electrodes

Received: July 5, 2018  
Revised: August 25, 2018  
Published online:

- [1] X. Ji, L. F. Nazar, *J. Mater. Chem.* **2010**, *20*, 9821.  
[2] X. Ji, K. T. Lee, L. F. Nazar, *Nat. Mater.* **2009**, *8*, 500.  
[3] a) Y. Liu, G. Li, J. Fu, Z. Chen, X. Peng, *Angew. Chem., Int. Ed.* **2017**, *56*, 1; b) W. Ahn, M. H. Seo, Y. S. Jun, D. U. Lee, F. M. Hassan, X. Wang, A. Yu, Z. Chen, *ACS Appl. Mater. Interfaces* **2016**, *8*, 1984; c) X. Wang, G. Li, J. Li, Y. Zhang, A. Wook, A. Yu, Z. Chen, *Energy Environ. Sci.* **2016**, *9*, 2533; d) B. Li, S. Li, J. Liu, B. Wang, S. Yang, *Nano Lett.* **2015**, *15*, 3073.

- [4] a) T. Yim, S. H. Han, N. H. Park, M.-S. Park, J. H. Lee, J. Shin, J. W. Choi, Y. Jung, Y. N. Jo, J.-S. Yu, K. J. Kim, *Adv. Funct. Mater.* **2016**, *26*, 7817; b) W. Ahn, S. Lim, D. Lee, K. Kim, Z. Chen, S. Yeon, *J. Mater. Chem. A* **2015**, *3*, 9461.  
[5] a) N. Azimi, Z. Xue, I. Bloom, M. L. Gordin, D. Wang, T. Daniel, C. Takoudis, Z. Zhang, *ACS Appl. Mater. Interfaces* **2015**, *7*, 9169; b) Z. Nan, L. Bin, L. Songmei, Y. Shubin, *Adv. Energy Mater.* **2018**, *8*, 1702754.  
[6] a) Y. Hwa, H. K. Seo, J.-m. Yuk, E. J. Cairns, *Nano Lett.* **2017**, *17*, 7086; b) J. Chen, W. A. Henderson, H. Pan, B. R. Perdue, R. Cao, J. Z. Hu, C. Wan, K. S. Han, K. T. Mueller, J.-G. Zhang, *Nano Lett.* **2017**, *17*, 3061.  
[7] Q. Pang, X. Liang, C. Y. Kwok, J. Kulisch, L. F. Nazar, *Adv. Energy Mater.* **2017**, *7*, 1601630.  
[8] M. Hagen, D. Hanselmann, K. Ahlbrecht, R. Maça, D. Gerber, J. Tübke, *Adv. Energy Mater.* **2015**, *5*, 1401986.  
[9] G. Li, Z. Chen, J. Lu, *Chem* **2018**, *4*, 3.  
[10] a) H. J. Peng, J. Q. Huang, X. B. Cheng, Q. Zhang, *Adv. Energy Mater.* **2017**, *7*, 1700260. b) S.-H. Chung, L. Luo, A. Manthiram, *ACS Energy Lett.* **2018**, *3*, 568; c) G. Li, W. Lei, D. Luo, Y. P. Deng, D. Wang, Z. Chen, *Adv. Energy Mater.* **2018**, *8*, 1702381; d) G. Li, W. Lei, D. Luo, Y. Deng, Z. Deng, D. Wang, A. Yu, Z. Chen, *Energy Environ. Sci.* **2018**, *11*, 2372.  
[11] S. H. Chung, A. Manthiram, *Adv. Mater.* **2018**, *30*, 1705951.  
[12] X. Yang, X. Li, K. Adair, H. Zhang, X. Sun, *Electrochem. Energy Rev.* **2018**, *1*, 239.  
[13] D. Lv, J. Zheng, Q. Li, X. Xie, S. Ferrara, Z. Nie, L. B. Mehdi, N. D. Browning, J. G. Zhang, G. L. Graff, *Adv. Energy Mater.* **2015**, *5*, 1402290.  
[14] M. Li, Y. Zhang, F. M. Hassan, W. Ahn, X. Wang, W. Liu, G. Jiang, Z. Chen, *J. Mater. Chem. A* **2017**, *5*, 21435.  
[15] Y. Ma, H. Zhang, B. Wu, M. Wang, X. Li, H. Zhang, *Sci. Rep.* **2015**, *5*, 14949.  
[16] D. Gueon, J. T. Hwang, S. B. Yang, E. Cho, K. Sohn, D.-K. Yang, J. H. Moon, *ACS Nano* **2018**, *12*, 226.  
[17] a) D. S. Jung, T. H. Hwang, J. H. Lee, H. Y. Koo, R. A. Shakoov, R. Kahraman, Y. N. Jo, M.-S. Park, J. W. Choi, *Nano Lett.* **2014**, *14*, 4418; b) J. Ma, Z. Fang, Y. Yan, Z. Yang, L. Gu, Y.-S. Hu, H. Li, Z. Wang, X. Huang, *Adv. Energy Mater.* **2015**, *5*, 1500046.  
[18] M. Li, Y. Zhang, X. Wang, W. Ahn, G. Jiang, K. Feng, G. Lui, Z. Chen, *Adv. Funct. Mater.* **2016**, *26*, 8408.  
[19] Y. Shen, T. Jing, W. Ren, J. Zhang, Z.-G. Jiang, Z.-Z. Yu, A. Dasari, *Compos. Sci. Technol.* **2012**, *72*, 1430.  
[20] a) M. Kuhnhen, T. V. Joensen, M. Reck, I. V. Roisman, C. Tropea, *Int. J. Multiphase Flow* **2018**, *100*, 30; b) F. E. Bastan, G. Erdogan, T. Moskalewicz, F. Ustel, *J. Alloys Compd.* **2017**, *724*, 586.  
[21] Z. Mao, M. Farkhondeh, M. Pritzker, M. Fowler, Z. Chen, *J. Electrochem. Soc.* **2016**, *163*, A458.  
[22] E. W. Washburn, *Phys. Rev.* **1921**, *17*, 273.  
[23] a) G. Tan, R. Xu, Z. Xing, Y. Yuan, J. Lu, J. Wen, C. Liu, L. Ma, C. Zhan, Q. Liu, T. Wu, Z. Jian, R. Shahbazian-Yassar, Y. Ren, D. J. Miller, L. A. Curtiss, X. Ji, K. Amine, *Nat. Energy* **2017**, *2*, 17090; b) Y. Yuan, G. Tan, J. Wen, J. Lu, L. Ma, C. Liu, X. Zuo, R. Shahbazian-Yassar, T. Wu, K. Amine, *Adv. Funct. Mater.* **2018**, *28*, 1706443.  
[24] Z. Deng, Z. Zhang, Y. Lai, J. Liu, J. Li, Y. Liu, *J. Electrochem. Soc.* **2013**, *160*, A553.  
[25] N. A. Cañas, K. Hirose, B. Pascucci, N. Wagner, K. A. Friedrich, R. Hiesgen, *Electrochim. Acta* **2013**, *97*, 42.  
[26] a) L. Yuan, X. Qiu, L. Chen, W. Zhu, *J. Power Sources* **2009**, *189*, 127; b) D.-R. Chang, S.-H. Lee, S.-W. Kim, H.-T. Kim, *J. Power Sources* **2002**, *112*, 452.  
[27] S. Jiao, J. Zheng, Q. Li, X. Li, M. H. Engelhard, R. Cao, J.-G. Zhang, W. Xu, *Joule* **2018**, *2*, 110.  
[28] a) D. Lv, J. Zheng, Q. Li, X. Xie, S. Ferrara, Z. Nie, L. B. Mehdi, N. D. Browning, J.-G. Zhang, G. L. Graff, J. Liu, J. Xiao, *Adv. Energy*

- Mater.* **2015**, *5*, 1402290; b) Q. Pang, L. F. Nazar, *ACS Nano* **2016**, *10*, 4111; c) Y. Zhong, X. Xia, S. Deng, J. Zhan, R. Fang, Y. Xia, X. Wang, Q. Zhang, J. Tu, *Adv. Energy Mater.* **2018**, *8*, 1701110.
- [29] F. Y. Fan, Y.-M. Chiang, *J. Electrochem. Soc.* **2017**, *164*, A917.
- [30] a) M. Holzappel, A. Martinent, F. Alloin, B. Le Gorrec, R. Yazami, C. Montella, *J. Electroanal. Chem.* **2003**, *546*, 41; b) J. Illig, M. Ender, T. Chrobak, J. P. Schmidt, D. Klotz, E. Ivers-Tiffée, *J. Electrochem. Soc.* **2012**, *159*, A952.
- [31] C. Shen, J. Xie, M. Zhang, J. P. Zheng, M. Hendrickson, E. J. Plichta, *J. Electrochem. Soc.* **2017**, *164*, A1220.
- [32] G. Li, X. Wang, M. H. Seo, M. Li, L. Ma, Y. Yuan, T. Wu, A. Yu, S. Wang, J. Lu, Z. Chen, *Nat. Commun.* **2018**, *9*, 705.
- [33] J. Conder, R. Bouchet, S. Trabesinger, C. Marino, L. Gubler, C. Villevieille, *Nat. Energy* **2017**, *2*, 17069.
- [34] J. Song, T. Xu, M. L. Gordin, P. Zhu, D. Lv, Y. B. Jiang, Y. Chen, Y. Duan, D. Wang, *Adv. Funct. Mater.* **2014**, *24*, 1243.